Temporal and spatial dependence of a yearlong record of sound propagation from the Canada Basin to the Chukchi Shelf

Megan S. Ballard, Mohsen Badiey, Jason D. Sagers, et al.

Citation: The Journal of the Acoustical Society of America **148**, 1663 (2020); doi: 10.1121/10.0001970
View online: https://doi.org/10.1121/10.0001970
View Table of Contents: https://asa.scitation.org/toc/jas/148/3
Published by the Acoustical Society of America

JASA ARTICLE

Temporal and spatial dependence of a yearlong record of sound propagation from the Canada Basin to the Chukchi Shelf[a)]

Megan S. Ballard,[1,b)] Mohsen Badiey,[2] Jason D. Sagers,[1] John A. Colosi,[3] Altan Turgut,[4] Sean Pecknold,[5] Ying-Tsong Lin,[6] Andrey Proshutinsky,[6] Richard Krishfield,[6] Peter F. Worcester,[7] and Matthew A. Dzieciuch[7]

[1]*Applied Research Laboratories, The University of Texas at Austin, Austin, Texas 78713, USA*

[2]*University of Delaware, Newark, Delaware 19716, USA*

[3]*Naval Postgraduate School, Monterey, California 93943, USA*

[4]*U.S. Naval Research Laboratory, Washington, D.C. 20375, USA*

[5]*Defence Research and Development Canada, Dartmouth, Nova Scotia, Canada*

[6]*Woods Hole Oceanographic Institution, Woods Hole, Massachusetts 02543, USA*

[7]*Scripps Institution of Oceanography, University of California at San Diego, La Jolla, California 92093, USA*

ABSTRACT:

The Pacific Arctic Region has experienced decadal changes in atmospheric conditions, seasonal sea-ice coverage, and thermohaline structure that have consequences for underwater sound propagation. To better understand Arctic acoustics, a set of experiments known as the deep-water Canada Basin acoustic propagation experiment and the shallow-water Canada Basin acoustic propagation experiment was conducted in the Canada Basin and on the Chukchi Shelf from summer 2016 to summer 2017. During the experiments, low-frequency signals from five tomographic sources located in the deep basin were recorded by an array of hydrophones located on the shelf. Over the course of the yearlong experiment, the surface conditions transitioned from completely open water to fully ice-covered. The propagation conditions in the deep basin were dominated by a subsurface duct; however, over the slope and shelf, the duct was seen to significantly weaken during the winter and spring. The combination of these surface and subsurface conditions led to changes in the received level of the sources that exceeded 60 dB and showed a distinct spacio-temporal dependence, which was correlated with the locations of the sources in the basin. This paper seeks to quantify the observed variability in the received signals through propagation modeling using spatially sparse environmental measurements. © *2020 Acoustical Society of America*. https://doi.org/10.1121/10.0001970

(Received 28 June 2020; revised 27 August 2020; accepted 28 August 2020; published online 23 September 2020)

[Editor: James F. Lynch] Pages: 1663–1680

I. INTRODUCTION

The Pacific Arctic Region has experienced changes in atmospheric conditions, seasonal sea-ice coverage, and thermohaline structure that have been well documented over the last 50 years and have important consequences for underwater sound. Sea-ice losses in the northern Chukchi and Beaufort Seas during the summer melt season have resulted in an increase in the ice-free ocean area of 70% compared to the climatological mean (Wood *et al.*, 2015). Furthermore, a doubling in Beaufort Gyre halocline heat content has been observed over the past three decades (Timmermans *et al.*, 2018). Both of these changes have implications for acoustic propagation: sound incurs less surface loss from open water than from the rough ice interface, and it is more efficiently channeled by warmer water in the upper halocline which forms the top boundary of a subsurface acoustic duct. Together, these changes are contributing to a significantly different acoustic propagation environment compared to that of previous decades.

In 2016 and 2017, a set of experiments known as the deep-water Canada Basin acoustic propagation experiment (CANAPE) and shallow-water Canada Basin acoustic propagation Experiment (SW CANAPE) was conducted in the Canada Basin and on the Chukchi Shelf. SW CANAPE took place over a yearlong period beginning in October 2016 and involved 22 moorings that included acoustic sources and receiver arrays as well as arrays of oceanographic sensors (Badiey *et al.*, 2019; Collins *et al.*, 2019). One of the experimental objectives of SW CANAPE was to assess the variability of acoustic receptions of signals generated by six deep-water CANAPE transceiver moorings in the basin and received on the shelf (Badiey *et al.*, 2014). In this paper, the measured acoustic data are used to explore the use of acoustic signals as a remote sensing tool in the transitioning Arctic. The principal components of deep-water CANAPE were six transceiver moorings and a distributed vertical line array (DVLA) that were deployed for a yearlong period beginning in September 2016.

This paper reports on receptions of low-frequency signals in the nominal frequency band 200–300 Hz from five of the six Scripps Institution of Oceanography (SIO) tomographic sources located in the Canada Basin that were

[a)]This paper is part of the special issue on Ocean Acoustics in the Changing Arctic.

[b)]Electronic mail: meganb@arlut.utexas.edu

recorded by the Applied Research Laboratories at the University of Texas at Austin (ARL:UT) Persistent Acoustic Observation System (PECOS) array of hydrophones located on the Chukchi Shelf. Seasonal changes in the received level (RL) on the order of 60 dB were observed for the signals from all five SIO sources. The case is made that the increase in transmission loss (TL) was caused by seasonal changes in both the oceanographic conditions and the sea ice cover. Analysis of the RL from the tomography sources revealed a spatial dependence in the onset of the seasonal increase in TL, which was correlated with the locations of the sources in the basin (Ballard *et al.*, 2019). A similar temporal-spatial pattern was observed when TL decreased during the summer melt season.

To support the acoustic propagation experiment, environmental measurements were made both in the Canada Basin and on the Chukchi Shelf. Water temperature and salinity were measured in the basin by the SIO DVLA and on the shelf by the University of Delaware (UD) array of oceanographic moorings, UD1 to UD7 (Badiey *et al.*, 2019). While the environmental data only exist on the shelf and in the basin, they collectively indicate that the range-dependent propagation conditions during the winter and spring change from predominately ducted in the basin to seasonally upward refracting on the continental shelf. Ice draft was measured in both deep and shallow locations by upward looking sonars (ULS). In the basin, each of the SIO tomography moorings included a Woods Hole Oceanographic Institution (WHOI) ULS, and on the shelf, ice draft was measured by the Naval Research Laboratory (NRL) ULS. This paper examines the temporal changes of the range-dependent measurements and seeks to explain the observed RL variability of the acoustic signals using these measurements with propagation modeling.

This paper has the following organization. Section II contains background information on the Arctic environment including the seasonal sea ice cover, oceanography of the northern Chukchi and Beaufort Seas, and important acoustic propagation effects. The CANAPE experiments are described in Sec. III and the acoustic measurements are examined in the context of the environmental measurements. Section IV applies an acoustic propagation model to calculate yearlong time-series data from the SIO sources and compares these time-series to the observations. Conclusions are discussed in Sec. V.

II. BACKGROUND

A. Sea ice conditions

The Arctic Ocean has experienced dramatic declines in sea ice cover with some of the largest reductions occurring in the Chukchi and Beaufort Seas. Changes associated with declines in sea ice extent include long-term thinning trends of sea ice, a lengthening of the summer melt season, and a shift from primarily perennial multi-year ice to seasonal first-year ice (Frey *et al.*, 2015; Krishfield *et al.*, 2014). The Arctic sound channel is largely upward refracting and so acoustic propagation is strongly affected by the the sea surface whose properties transition over the course of the yearlong CANAPE, progressing from open water, through the ice growth period, to full cover by pack ice, and through the melt season back to ice-free conditions. In addition to the seasonal presence of the ice, the physical properties of the ice as well as the topography of the ice canopy influence acoustic propagation through loss and scattering mechanisms. This section provides an overview of the sea ice characteristics and describes their effects on acoustic propagation.

Sea ice cover across the Chukchi and Beaufort Seas is seasonally variable, with much of the area covered primarily with first-year ice, but also including small amounts of multi-year sea ice for several months of each year. Based on satellite data collected between 2003 and 2010, on average, sea ice freeze-up occurs in most of the areas in the Canada Basin by the end of October and in the Chukchi Sea by the end of November. Patterns in the timing of breakup roughly follow latitude, except in cases where winds open localized polynyas, such as the southeastern Beaufort Sea (Frey *et al.*, 2015). The most persistent ice is located in the northeastern sector of the Beaufort near the Canadian Archipelago.

Over large areas, sea ice is generally not flat and on average consists of 10%–40% ridges by volume (Strub-Klein and Sudom, 2012). Sea ice ridges are formed when ice floes collide, resulting in ice deformation by rafting, ridging, or rubbling. Scattering loss is dependent on the topography of the under-ice surface, and it can dominate the intrinsic reflection loss. Scattering loss is a function of both the acoustic frequency and angle of the incident wave impinging on a rough surface. Using an analytical model for perfectly reflecting ridges shaped as elliptic half-cylinders, Diachok (1976) showed the scattering loss could exceed 10 dB for grazing angles below 5° and frequencies above 50 Hz. This is significantly greater than the reflection loss of 2 dB calculated over the same range of grazing angles by McCammon and McDaniel (1985) due to the intrinsic properties of the sea ice.

B. Oceanographic conditions

Acoustic propagation is influenced by the depth-dependent structure of sea water temperature and salinity, which determine sound speed, as well as the spatial and temporal variability of these properties as dictated by ocean dynamic processes including currents, eddies, internal waves, and density-compensated fine structure (spice). This section briefly describes the prevailing oceanography within the northern Chukchi and Beaufort Seas and the effects on acoustic propagation.

As illustrated by Fig. 1, Pacific water enters the Arctic Ocean through the Bering Strait, from which it flows primarily northward across the wide and shallow Chukchi Sea. During winter months, the Pacific-origin water is cooled on the Chukchi Shelf forming the Pacific Winter Water (PWW) mass, while during summer months it is warmed by solar

https://doi.org/10.1121/10.0001970

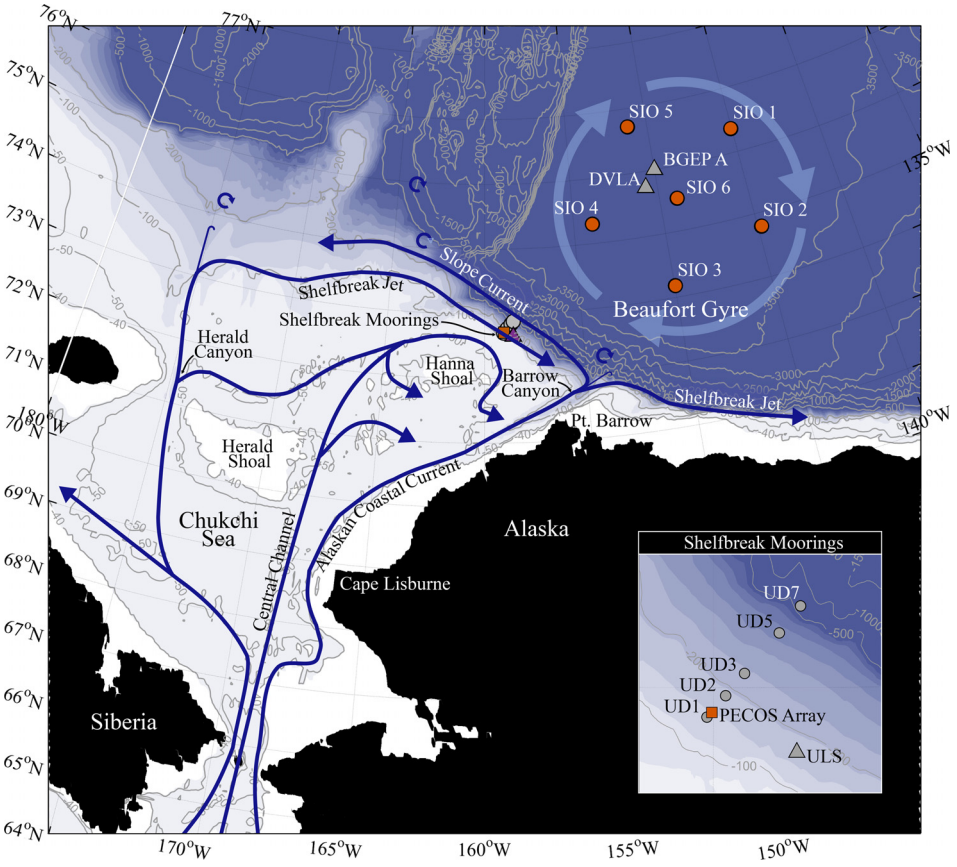

FIG. 1. (Color online) Schematic of circulation in the Chukchi Sea and western Beaufort (based on Corlett and Pickart, 2017), showing the three main pathways by which Pacific water flows poleward through the Chukchi Sea. The locations of the SIO tomographic sources in the Canada Basin and the ARL:UT PECOS array on the Chukchi Shelf are indicated by orange markers, and the locations of the environmental measurements including the BGEP Mooring A and the SIO DVLA in the Canada Basin and the array of UD oceanographic moorings on the shelf are shown by gray markers. The inset map shows a close-up view of the shelfbreak moorings.

irradiation and river runoff forming the Pacific Summer Water (PSW) mass (Brugler *et al.*, 2014). The Pacific-origin water is eventually transported into the Canada Basin where it becomes the principal component of the halocline in approximately the upper 250 m. The warmer and less saline PSW overlies the cooler PWW. Above the PSW and below the ice canopy is a surface mixed layer of near constant temperature and salinity. Below the PWW is warm, saline water originating from the Atlantic Ocean. The Beaufort Gyre, a large wind-driven current, controls the large-scale circulation of the water masses in the Canada Basin.

Sound speed profiles computed from temperature and salinity profiles in the Canada Basin can show a sound speed minimum known as the Beaufort Duct (Duda, 2017) or Beaufort Lens (Lynch *et al.*, 2018), which lies between the PSW and the Atlantic Layer. Sound paths launched horizontally from a source located in this duct are partially shielded from interaction with the ice, experience lower TL, and can be detected at greater distances. This duct has enabled long-range under-ice navigation and data transmission in the Beaufort Sea (Freitag *et al.*, 2015). The extent to which sound is trapped in the acoustic duct depends on the acoustic frequency, and sound is not efficiently channeled below a modal cutoff frequency. The rate of change of TL within the duct depends on the temperature of the PSW layer, which forms its upper boundary and exhibits spatial and temporal variability. An examination of ice-tethered profiler (ITP) data collected between 2002 and 2015 in the Beaufort Sea (Krishfield *et al.*, 2008; Toole *et al.*, 2011), revealed that the propagation conditions for the deep-water CANAPE sources can vary from strongly ducted to upward refracting and surface interacting. Using the measured ITP profiles, predictive modeling by Sagers *et al.* (2015), demonstrated that details of the range-dependence of the PSW layer can lead to TL variability from 20 to 40 dB. Later, using a surface-forced hydrodynamic model of the region, Duda *et al.* (2019) showed that eddies and filaments strengthen and weaken the duct leading to TL fluctuations of approximately 35 dB. In both modeling studies, the large increases in TL resulted from discontinuities in the upper boundary of the subsurface duct that allowed sound to escape and interact with the ice cover.

Within the vicinity of the hydrophone array on the Chukchi Shelf, two currents play an important role in transporting Pacific-origin water and influencing acoustic propagation during certain months of the year. A portion of the water from the western branch flowing through Herald Canyon is channeled eastward and flows as the narrow, bottom-intensified Chukchi Shelfbreak Jet near the location of the PECOS array. Further offshore, the Chukchi slope current flows westward from Barrow Canyon as a surface-intensified free jet. These currents are labeled in Fig. 1, and their approximate locations are shown near the PECOS array.

The Chukchi Slope Current is centered offshore of the shelfbreak jet with its strongest mean flow within 25 km of the shelfbreak and significant flow out to 60 km offshore (Corlett and Pickart, 2017). Its northern edge is estimated at 100 km

offshore of the shelfbreak. Seasonally, the slope current is surface-intensified (with a maximum speed on the order of 20 cm/s at the core) in summer and autumn, and becomes mid depth-intensified in winter and spring with a weaker speed (order 10 cm/s at the core) (Li *et al.*, 2019). The seasonal changes in the speed of the slope current are related to the volume transport and direction of the offshore flow from Barrow Canyon. The outflow is stronger to the east in winter/spring, and during this period most of its outflow is distributed to the Beaufort Shelfbreak Jet; it is stronger to the west in summer/fall, when the majority of its outflow goes into the Chukchi slope current (Spall *et al.*, 2018).

The hydrographic time series from Li *et al.* (2019) reveals the seasonality of water masses in the Chukchi slope current. Throughout the fall and into the early winter, PSW is advected by the slope current, and a temperature minimum capable of supporting ducted sound propagation is present. During the early winter, newly-ventilated Winter Water (WW) appearing in the upper 50–75 m, which is likely the signature of convective overturning driven by brine rejection as a result of re-freezing polynyas, weakens the upper boundary of the acoustic duct for short periods. The WW mass is the coldest type of Pacific water, and it is defined as having temperatures below –1.6 °C. As the season progresses, the temperature of this water mass is moderated, at which point it is referred to as Remnant Winter Water (RWW) (Corlett and Pickart, 2017, and references therein). Li *et al.* (2019) found that WW in the depth range of 50 m to 170 m first appeared in March and lasted until the end of August, with a large and continuous amount of WW present from early-April to late-July. During this time period, the upper boundary of the acoustic duct vanishes, and the water-column sound-speed profile is upward refracting. The disappearance of the acoustic duct in the Chukchi Slope Current has significant implications for acoustic propagation, as will be discussed in detail in Sec. IV. Using observations from the SW CANAPE sources and receivers on the Chukchi Shelf, for example, Badiey *et al.* (2019) showed a 20 dB change in the RL that was correlated with the occurrence of an oceanographic event spanning the upper 150 m water column caused by a Pacific Water outflow from the Bering Sea and the retreat of the Marginal Ice Zone.

III. DATA

SW CANAPE was a multi-institutional acoustical oceanographic experiment, which was conducted by ARL:UT, UD, NRL, WHOI, and Defence Research and Development Canada (DRDC). This section examines the signals that were transmitted from deep-water CANAPE SIO tomographic sources and received by PECOS, one of several hydrophone arrays on the Chukchi Shelf, during the yearlong experiment.

A. Acoustic measurements

The deep-water CANAPE SIO tomographic sources were deployed in the Canada Basin and began broadcasting a scheduled sequence of signals, which was repeated every four hours, immediately following their deployment in August 2016. The sources were shutdown and ceased broadcasting on 1 September 2017. The SW CANAPE moorings were deployed on the Chukchi Shelf in the latter part of the open water season, and the PECOS array began recording the SIO signals on 25 October 2016. PECOS was limited to a 24 min recording period six times per day, which did not enable the reception of all six SIO signals for every broadcast sequence. To accommodate the desire to monitor all six propagation paths, PECOS shifted its recording schedule to measure signals from the first four SIO sources and the last four SIO sources in alternate recordings. Hence, signals from SIO 1 and SIO 2 can only be observed in the odd-numbered recordings, signals from SIO 5 and SIO 6 can only be observed in the even-numbered recordings, and signals from SIO 3 and SIO 4 can be observed in all recordings. The combined broadcasting and recording schedules produced a record of received signals that is 10 months and 25 days in duration and consists of 2082 recordings that may include receptions of the SIO signals depending on the signal-to-noise ratio.

As shown in Fig. 1, the SIO sources were arranged in a pentagon pattern within the deepest part of the Canada Basin where the water depth was approximately 3800 m. The distance from the sources to the PECOS array ranged from 238 to 517 km as listed in Table I. The sources were deployed at a nominal depth of 175 m so that they were located within the Beaufort Duct. However, strong currents within the basin pulled the sources out of the duct for periods of days to months at a time. The depths of the sources recorded throughout the duration of the yearlong experiment are shown in Fig. 2.

Each of the SIO sources broadcast a 135 s-long linear frequency modulated (LFM) signal. With the exception of SIO 2, the signals had a center frequency close to 250 Hz

TABLE I. Characteristics of the SIO tomography sources.

SIO Mooring	Latitude (°N)	Longitude (°W)	Distance (km)	Center freq. (Hz)	Bandwidth (Hz)	SL (dB)
SI0 1	75.3632	145.0522	517	255	100	184
SI0 2	73.7870	144.8043	470	172.5	65	184
SI0 3	73.1807	149.9738	299	275	100	184
SI0 4	74.3018	153.9499	238	275	100	183
SI0 5	75.7177	151.1767	410	250	100	184
SI0 6	74.5027	149.0122	373	255	100	N/A

https://doi.org/10.1121/10.0001970

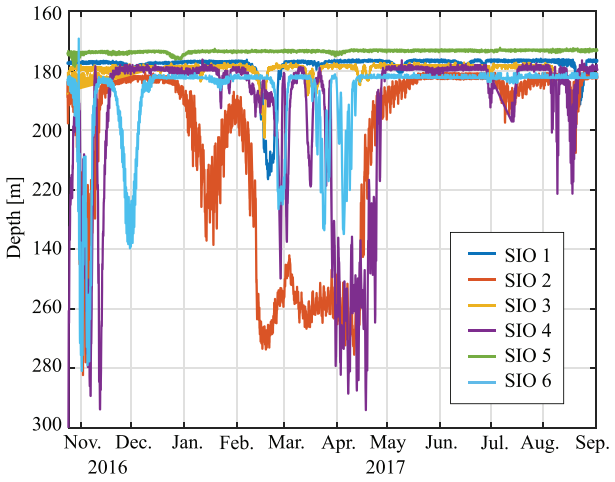

FIG. 2. (Color online) Measured depths of the SIO tomography sources throughout the experiment.

and a 100 Hz bandwidth. SIO 2 was lower in frequency and a had proportionally narrower bandwidth. The center frequency, bandwidth, and source level (SL) of each source are listed Table I. Shortly after deployment, SIO 6 malfunctioned, and it broadcast a low SL signal that could not be detected on the Chukchi Shelf. The signals from the remaining five sources are considered in the subsequent analysis.

The SIO signals were received by hydrophones in the horizontal line array (HLA) and recorded by PECOS. The 34-element HLA was designed as a 220 m-long center-tapered array, and the data were recorded at a sampling rate of 8192 Hz. The HLA was deployed at 72.7105° N, 159.0100° W on the 150 m isobath with broadside (defined as 0°) oriented toward the center of the SIO pentagon of tomography sources. The measured signals were pulse compressed and conventional frequency-domain beamforming was applied using 0.5 s integration time with 75% overlap. The resulting beamformed, pulse-compressed data are shown in Fig. 3 with the time elapsed after the signal was emitted on the *y*-axis and the time of year of the *x*-axis. For each reception, two groups of acoustic arrivals can be observed, as indicated by the numbered markers in the figure. The first group of arrivals is composed of high angle arrivals that interact with the waveguide boundaries. Although these arrivals travel a greater cumulative distance

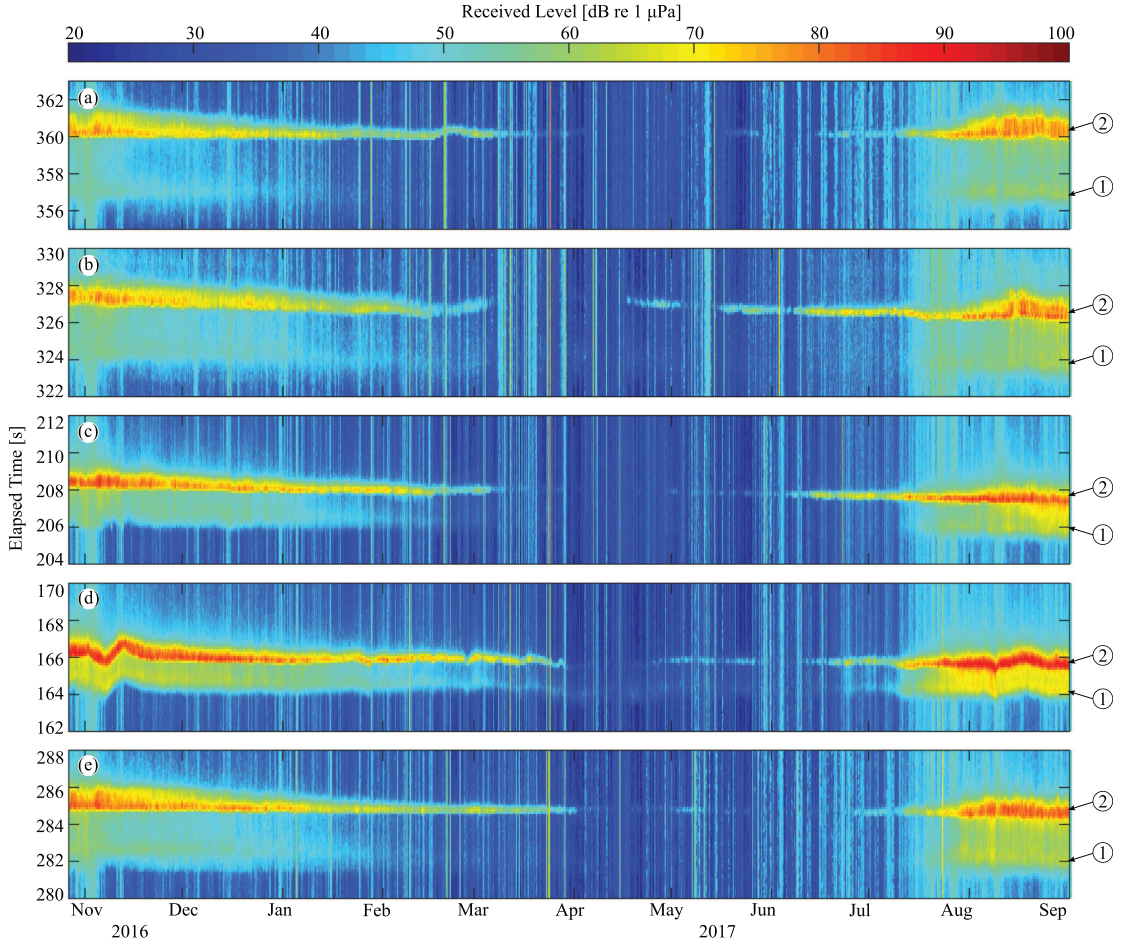

FIG. 3. (Color online) Beamformed pulse-compressed arrivals of the signals from (a) SIO 1, (b) SIO 2, (c) SIO 3, (d) SIO 4, and (e) SIO 5 recorded by PECOS. For each reception, the first group of arrivals (labeled 1), are composed of high angle arrivals that interact with the waveguide boundaries, and the latter group of arrivals (labeled 2) is composed of low angle arrivals that propagate through the sound-speed duct in the Canada Basin. These data have not been corrected for mooring motion.

along the ray paths, they arrive first because they travel at a greater average speed than the ducted arrivals. The later group of arrivals is composed of low angle arrivals that propagate through the sound-speed duct in the Canada Basin. They have a greater amplitude because they incur less loss from surface interactions. An acoustic propagation model will be applied to demonstrate these effects in Sec. IV.

The seasonal dependence of RL can be clearly observed in Fig. 3. Over the course of the yearlong experiment, the dynamic range of the RL from all five sources is on the order of 60 dB. The RL is observed to decrease through the fall and winter, with the RL of the ducted arrival falling below the ambient noise level between March and April. For the more distant sources, there are periods of a month or more for which the signals cannot be detected. In May and June, the signal receptions are periodically masked by ambient noise events. The signal level increases in July and the highest RLs are observed during the open water season in August.

Both the SIO tomography sources and the PECOS array were equipped with atomic clocks, making it possible to monitor the arrival time of the SIO signals over the course of the yearlong experiment. Overall, the arrival time of the signals shows little variation over the course of the year. The fluctuations observed in Fig. 3 (i.e., SIO 1 and SIO 2 in February, SIO 4 in November) are primarily due to source motion, as currents in the basin pulled the moorings away from their nominal location. The associated depth excursions of the source displaced it from the sound speed duct (see Fig. 2), which also resulted in increased propagation loss.

To further investigate the seasonal dependence and make comparisons of the temporal changes in the RL along the five propagation paths, relative TL was computed for all signal receptions. The TL for each reception was determined by subtracting the peak RL from the known SL. Prior to CANAPE, the SIO sources were calibrated at Lake Seneca, and their nominal measured SL is used in these calculations. The peak RL was calculated from the maximum of the pulse-compressed beamformed time series, excluding receptions for which the RL was lower than the ambient noise level. Relative TL was calculated by normalizing TL throughout the year such that the average TL during the open-water condition in August was set equal to zero. Relative TL from all five SIO tomography sources is shown in Fig. 4. Receptions from all five moorings display the seasonal increase in TL during the fall and winter and a decrease in TL in the summer. Moreover, it is evident from Fig. 4 that the onset of the increase/decrease in TL is correlated with position. Receptions from the most eastern mooring, SIO 3, experience the change in propagation conditions more than a month before the receptions from the westernmost mooring, SIO 5. This can be most easily observed during the months of February and March when TL increases rapidly for receptions of signals from all five moorings, and during the months of June and July when TL decreases back to that of open water conditions. An additional observation is that the rate of decrease in TL appears faster for the western moorings. For receptions from all sources, TL temporarily decreases for periods between April and June. The data also show short time variations in the RL, that include a range of up to 10 dB from one reception to the next.

B. Environmental measurements

Environmental measurements, including ocean temperature, salinity, and sea ice draft, were collected at each of the locations of the SIO sources and at several locations on the Chukchi Shelf. However, the full coverage between the

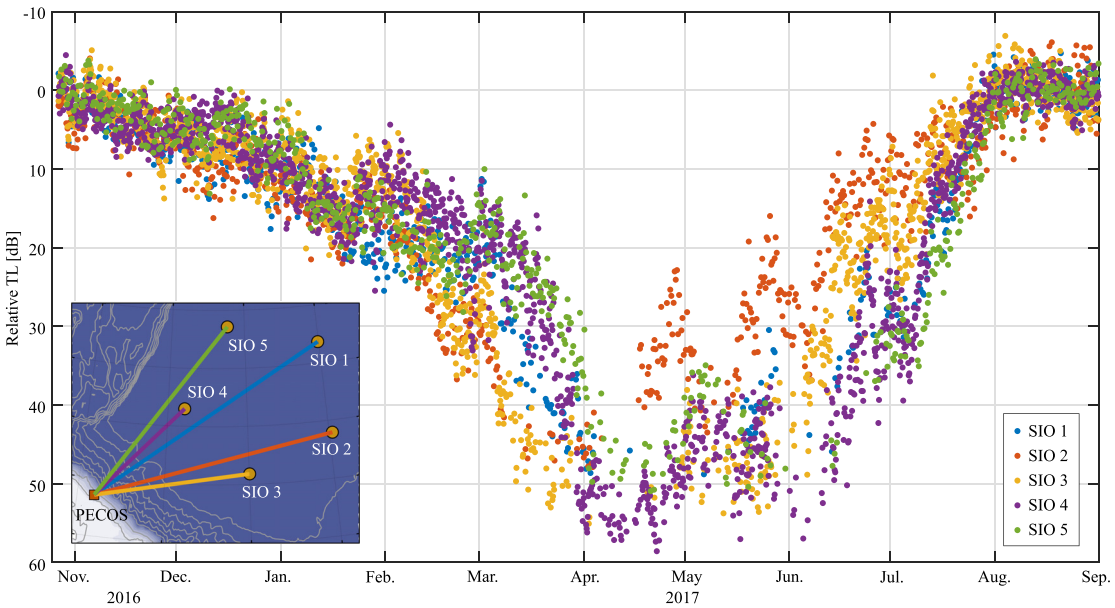

FIG. 4. (Color online) Relative TL calculated for the receptions from the SIO sources recorded by PECOS. The inset map shows the locations of the acoustic propagation paths for each of the receptions.

https://doi.org/10.1121/10.0001970

deep-water CANAPE and the SW CANAPE experiments was prohibitive due to the finite number of moorings deployed in this field experiment. The following sections describe the environmental measurements.

1. Water column measurements

Ocean temperature and salinity were measured on the Chukchi Shelf by UD1 to UD7, whose locations are shown by the inset map in Fig. 1. The locations of UD4 and UD6 are omitted as they did not provide data for this analysis. Temperature measurements were collected with Sea-Bird temperature sensors (SBE 56), which were spaced every 15 m for depths shallower than 300 m, and every 30 m for the deeper sections of the offshore moorings. Each mooring also contained up to two Sea-Bird MicroCATs (SBE 37-SMP), located near the upper and lower extents of the moorings, which measured salinity and pressure as well as temperature.

Temperature profiles measured by UD1–UD7 are shown in Fig. 5. Consistent with previous observations (Li *et al.*, 2019), the hydrographic data show the arrival of newly ventilated WW (shown in purple) first appearing in March and lasting until the end of June. The greatest volume of WW is observed in the inshore measurements. Measurements made at the deepest mooring locations only show significant quantities of WW in late March through early April. The arrival of PSW can be observed in July through September, with the greatest quantities observed at the locations of the offshore moorings. The PSW first appears near a depth of 100 m at UD3, UD5, and UD7, and then expands to fill the upper portion of the water column as the season progress and the current the transitions from mid-depth to surface intensified.

Within the Canada Basin, measurements of temperature and salinity were obtained from two adjacent moorings, the DVLA and the Beaufort Gyre Exploration Project (BGEP) Mooring A, whose locations are shown in Fig. 1. The DVLA was deployed by SIO as part of CANAPE and contained 25 Naval Postgraduate School (NPS) SBE 37-SMP between approximately 50 and 400 m depth that recorded at a sampling period of 5 min. In early May 2017, the pressure sensors on a subset of the SBE 37-SMP malfunctioned, and the data for this time period are displayed using a pressure

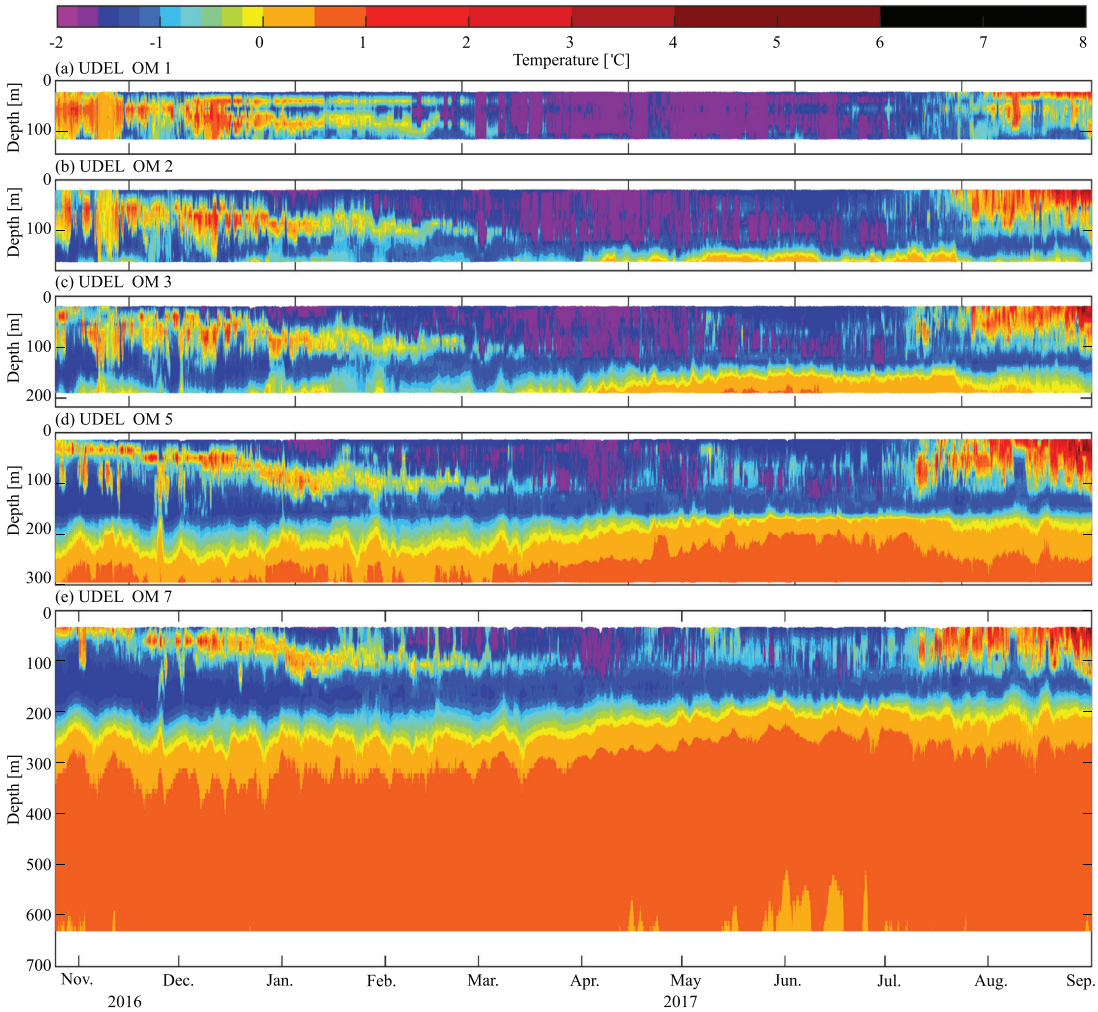

FIG. 5. (Color online) Temperature measured by the array of UD oceanographic moorings on the Chukchi Shelf and Slope. The moorings were located on 145, 179, 218, 350, and 704 m isobaths.

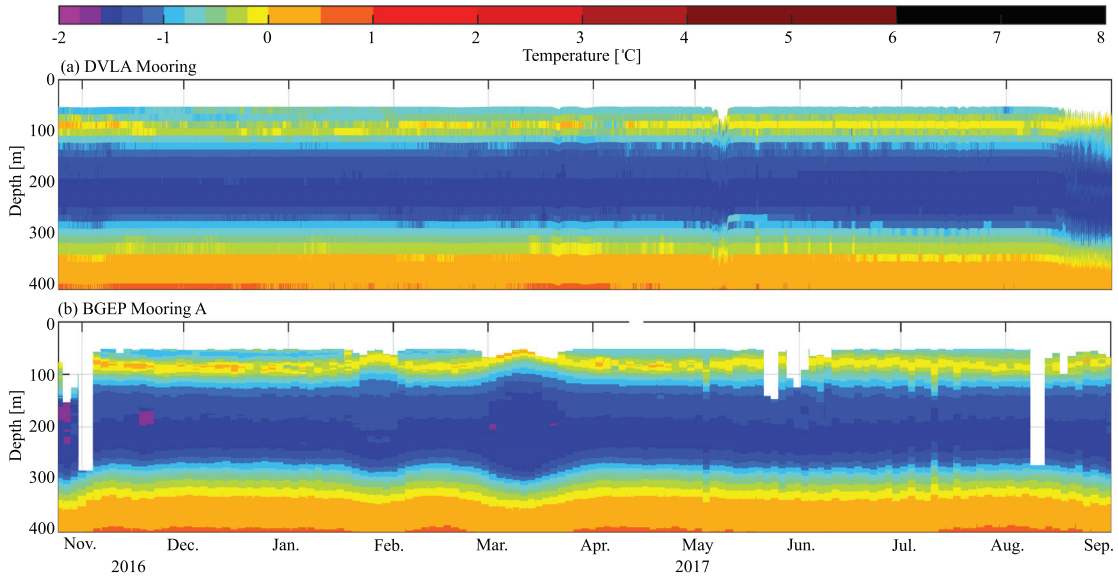

FIG. 6. (Color online) Temperature measured in the Canada Basin by (a) fixed sensors on the DVLA, and (b) the MMP on the BGEP Mooring A.

measurement from a reliable SBE 37-SMP and the known spacing between the sensors. BGEP Mooring A was deployed by WHOI as part of the BGEP (Proshutinsky *et al.*, 2019) and uses a McLane Moored Profiler (MMP) that measures conductivity, temperature, depth. MMP profiles are alternately separated by 6 and 48 h, spanning an approximate depth range of 50–2000 m. The two data sets are complementary: the fixed-depth sensors on the DVLA provide a finer temporal sampling of the water column, and the BGEP measurements provide a finer depth sampling. The temperature profiles measured by both systems during the period of CANAPE are shown in Fig. 6.

Both the DVLA and BGEP data sets show the consistent presence of the temperature minimum associated with a sound speed duct throughout the course of the yearlong CANAPE. While the measurements from the DVLA appear quiescent during the yearlong recording period, the data from the BGEP, measured less than 35 km away, are more variable and include the presence of several eddies (Proshutinsky *et al.*, 2020; Timmermans *et al.*, 2008; Zhao *et al.*, 2014; Zhong *et al.*, 2019).

2. Sea ice measurements

Figure 7 shows the daily mean and daily max ice draft measured by the ULS in the basin and on the shelf. The WHOI ULS on the basin moorings are sampled every 2 s and have a beam footprint of approximately 2 m (Krishfield *et al.*, 2014). The ULS measurements were made on all six SIO source moorings, but are missing for periods when

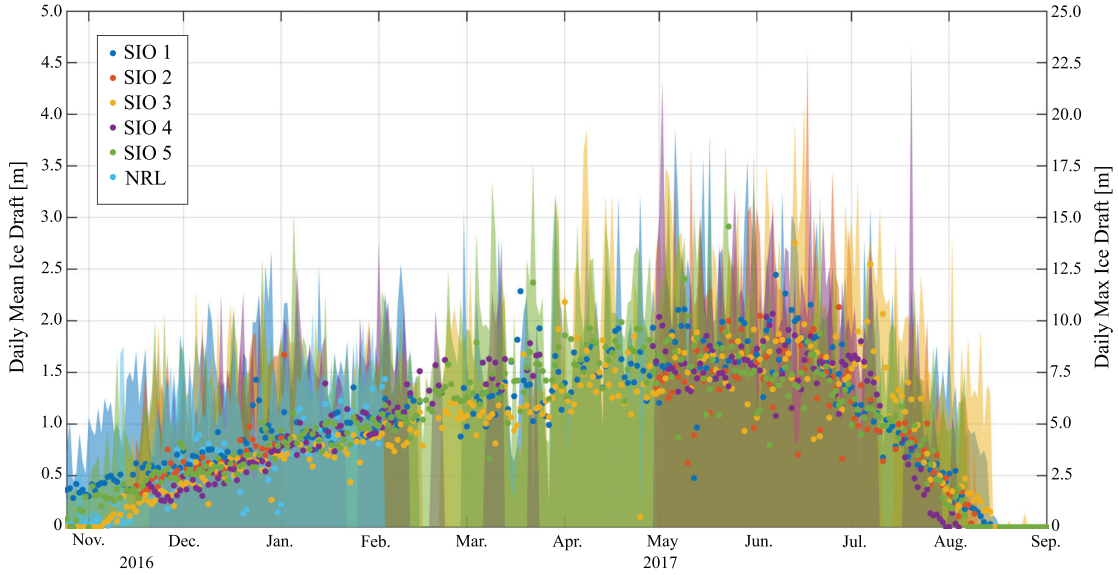

FIG. 7. (Color online) Daily mean ice draft (dots) and daily max (shaded areas) recorded by WHOI ULS on the SIO moorings in the basin and by ULS on the NRL mooring on the shelf.

https://doi.org/10.1121/10.0001970

currents on the mooring line pulled the ULS away from the ice canopy. The NRL ULS on the shelf sampled the ice draft every second but stopped recording at the beginning of February. At the beginning of the measurement period, the daily mean ice thickness is greatest for the northernmost mooring locations with open water still present for the SIO 3 measurement location and on the shelf. For all moorings, a gradual increase in ice thickness is observed between November and April, at which time the ice reaches its maximum daily mean thickness. At this time, the thickness of the undeformed sea ice is approximately 1.3 m, calculated from the median value of the ice draft. During this period, ice keels with drafts greater than 15 m are routinely observed in the measurements from all five basin moorings. After mid-June, the ice begins to melt, and the mean ice draft rapidly decreases. The daily maximum draft appears to decrease abruptly in mid-August and transition to open water as isolated floes dominate this metric.

C. Discussion

Comparison of the relative TL in Fig. 4 to the environmental measurements reveals some potential relationships between the data sets. Specifically, the rapid increase in TL that occurs in March is temporally correlated with the arrival of newly ventilated WW on the shelf and slope (see Fig. 5). The WW in the upper portion of the water column produces an upward refracting sound speed profile that results in increased interaction of sound with the ice canopy. This produces increased TL through the scattering of sound away from specular angles and conversion of acoustic waves propagating in the water to shear waves propagating in the sea ice. Although the thickness of the sea ice is also increasing during this period, as shown by the daily mean ice draft data shown in Fig. 7, the gradual increase in the thickness of the ice cover does not match the trend of the rapid increase in TL observed during the month of March.

Furthermore, the spatial dependence of the timing of the increase in TL can be explained by advection of the WW by the Chukchi Slope Current. This water mass exits the Chukchi Sea through Barrow Canyon and then flows westward transported by the Chukchi Slope Current. Recalling the experiment geometry in Fig. 1 (also see the inset map in Fig. 4), the acoustic propagation paths are spread over the slope so that water from the westward flowing slope current reaches the propagation path between SIO 3 and PECOS first, followed by the paths from SIO 2, SIO 1, SIO 4, and SIO 5.

Following this explanation, it is possible to estimate the speed of the Chukchi Slope Current from the acoustic data using the relative timing of the increase in TL and relative position of the propagation paths over the slope. Both the timing of the increase in TL and positions of the propagation paths were calculated relative to the SIO 1 data (see Table II). The timing in the increase in TL was determined from the mean time of observations of the relative TL spanning 25–40 dB between February 1 and April 1 shown in Fig. 4.

TABLE II. Estimating the speed of the Chukchi Slope Current.

Relative to SIO 1	Along shelf distance (km)	Increase in TL time (days)	Slope current speed (cm/s)
SI0 2	21.5	−16	1.6 ± 0.71
SI0 3	30.4	−23	1.5 ± 0.67
SI0 4	9.6	+6	1.9 ± 1.21
SI0 5	18.5	+12	1.8 ± 0.87

An uncertainty in the relative timing of three days arises from the horizontal scatter in the relative TL data. The along shelf distances between the propagation paths were calculated by assuming the midpoint of the slope current was located 60 km offshore of the 150 m isobath based measurements from Corlett and Pickart (2017). An uncertainty of 25 km in the location of the midpoint of the slope current was assumed based on the variability in the observations.

Using these data, the speed of the Chukchi Slope Current was estimated by dividing the relative along shelf distance by the relative timing of the increase in TL. The estimated speeds for each of the paths span a relatively small interval with an average value of 1.7 ± 0.86 cm/s. This estimate provides a range-integrated estimate of the current's speed, averaged over the lengths of the along shelf distances between the acoustic propagation paths.

The acoustically determined current speed is consistent with measurements reported by Stabeno *et al.* (2018) using an upward looking Acoustic Doppler Current Profiler (ADCP) moored on the 950 m isobath about 90 km east of the PECOS array. The ADCP measurements were acquired over a year-long period spanning 2014–2015. Although these data were collected in a different year and at a different location, they display a general pattern of circulation that can be compared to the SW CANAPE measurements. An annual minimum in the current speed of 2.5 cm/s was observed beginning in late March and persisting through the month of April. The magnitude of the measured speed is within the uncertainty of the acoustically determined value for this time of year.

A second major feature of the data shown in Fig. 4 is the decrease in relative TL that occurs during the months of June and July. The oceanographic data on the shelf and slope do not explain this phenomenon, since the arrival of PSW is not observed until mid-July. However, the timing of the decrease in relative TL is well-correlated with the timing of the ice melt as indicated by the daily mean ice draft measurements shown in Fig. 7. The propagation conditions remain upward refracting on the shelf and slope during this time period, but the diminishing ice canopy decreases the TL. The spatial dependence of the timing of the decrease in TL is explained by the pattern of the ice break up, which is influenced by a large localized polynya opened by winds in the southeastern Beaufort Sea (Frey *et al.*, 2015). Satellite data document a large crack that developed from the Beaufort Sea to the Lincoln Sea in May 2017 during the CANAPE measurements (see Mm. 1). No longer attached to the shoreline of the Canadian Arctic Archipelago, the ice

rotated with the Beaufort Gyre exposing the eastern moorings to open water conditions first.

Mm. 1. Satellite data document a large crack that developed from the Beaufort Sea to the Lincoln Sea in May 2017 during the CANAPE measurements. Locations of the SIO sources (orange circles) and PECOS array (orange square) are overlaid. Satellite data obtained from NASA Worldview Snapshots.

To quantify the spatial variability in the timing of the sea ice breakup across the Pacific Arctic Region, satellite data from the MASIE-AMSR2 (MASAM2) database (Fetterer *et al.*, 2015) were analyzed. For each pixel in the map shown in Fig. 8, the timing of the breakup was determined as the first date a pixel registered below an 85% sea ice concentration threshold. Spatial smoothing was applied to remove discontinuities in the data caused by spurious transient features in the satellite data. Compared to other studies, which have used a 15% sea ice concentration threshold, this work chose an 85% threshold because acoustic data appear to be more sensitive to this metric, showing significantly larger spread in the timing in the decrease in TL across the signals from the SIO sources during the beginning of the melt season (see Fig. 4). As shown in Fig. 8, the sea ice breakup is observed first at the locations of the easternmost moorings (i.e., SIO 2 and 3) and then progresses westward towards SIO 4 and 5. The trends in the timing of the sea ice breakup estimated from the satellite data generally agree with that of the decrease in TL observed in the signals from the SIO sources as shown in Fig. 4.

Although these observations lend some understanding into the environmental effects on TL, the acoustic propagation conditions are simultaneously influenced by both the presence of the ice cover, which causes increased loss due to surface scattering, and the water column properties, which can insulate the acoustic field from surface loss when the sound speed profile is downward refracting. To investigate the interrelationship between these effects, acoustic propagation modeling was carried out using the environmental measurements to inform the analysis.

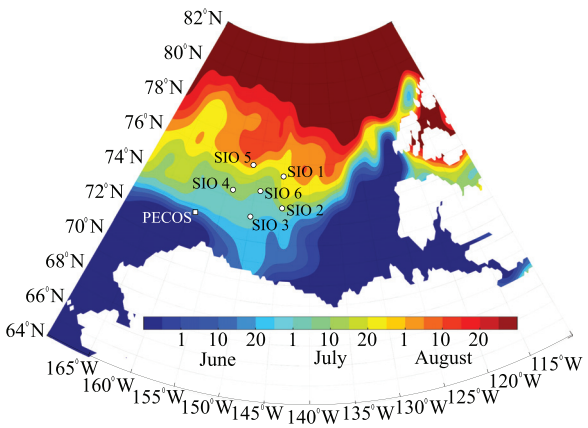

FIG. 8. (Color online) Timing of sea ice breakup across the Pacific Arctic Region. Values are based on an 85% sea ice concentration threshold using MASIE-AMSR2 (MASAM2) satellite time series.

IV. ACOUSTIC PROPAGATION MODELING

Acoustic propagation models to calculate the sound pressure field under sea ice have been studied for decades, and a variety of techniques have been proposed, including analytical (Diachok, 1976; Twersky, 1957) and approximate scattering models (Hope *et al.*, 2017; Kudryashov, 1996; LePage and Schmidt, 1994), as well as modal approaches (Ballard, 2019; Gavrilov and Mikhalevsky, 2006), parabolic equation (PE) models (Collins, 2015; Collins *et al.*, 2019; Collis *et al.*, 2016; Woolfe *et al.*, 2016), ray models (Sagers *et al.*, 2015), finite element (Simon *et al.*, 2018) and finite difference methods (Frick, 1991). The approaches can be divided into two broad classes: those that model interaction with the sea canopy using a reflection coefficient that encompasses both the average physical properties of the sea ice and statistics of its roughness, and those that model the full field using realizations of the sea ice that include its inhomogeneous internal properties and range-dependent topography.

This work uses the ray model Bellhop (Porter and Bucker, 1987) with scattering losses due to interaction with the sea ice canopy included through a range-dependent surface reflection coefficient. Ray theory is an approximate solution to the wave equation, and this modeling approach was chosen for its capability to handle range-dependent environments, its numerical stability, and its computational efficiency. However, in this application, there are inaccuracies related to the frequency-dependent extent to which sound is trapped within the sound speed duct. The ray solution includes rays that are fully trapped within the duct that do not incur surface loss. However, the low-frequency SIO source signals are not fully trapped in the duct, and they accumulate loss as they propagate through the Beaufort Sea. Nevertheless, the calculated TL reproduce many of the features observed in the measured data, including the spatial dependence in the onset of the seasonal increase in TL.

The calculation for surface loss is loosely based on an empirical model derived from historical data defined by Gordon and Bucker (1984). The inputs to the modified surface loss model are the standard deviation of the ice draft σ and the center frequency of the source signals. The reflection coefficient R in dB is calculated by

$$R(\sigma,f) = 0.00190\, f(2\sigma)^{1.5} \quad \text{for} \quad f \le 403(2\sigma)^{-0.5}$$
$$R(\sigma,f) = 0.541\, f(2\sigma)^{1.5} \quad \text{for} \quad f > 403(2\sigma)^{-0.5}. \qquad (1)$$

This surface loss model is approximate in the sense that it does not account for dependence on sea ice thickness, mechanical properties, spatial correlation length of the roughness, and other characteristics that are important in determining the reflection coefficient. However, given the spatial sparsity of the ice draft measurements, this simple

https://doi.org/10.1121/10.0001970

empirical model is applied to approximate surface loss as a function of acoustic frequency and ice draft.

Each set of calculated ray arrivals is described by a complex amplitude and travel time. The time-domain representation for the received waveform was calculated from these arrivals through application of the convolution theorem (Siderius *et al.*, 2007). A short-time Fourier transform with a 0.5 s time window and 75% overlap was applied to the calculated time series for comparison with the measured data, which were beamformed in the frequency domain using 0.5 s integration time (see Sec. III A). The calculated RL was obtained by subtracting the calculated TL from the known SL listed in Table I.

For each eight-hour period of the yearlong experiment, the Bellhop model was applied to calculate a set of ray arrivals. Although the signals were transmitted every four hours, due to the recording schedule of PECOS, receptions from SIO 1, SIO 2, and SIO 5 were only measured every eight hours. Although all receptions from SIO 3 and SIO 4 were recorded, the model is not capable of reproducing the short-term fluctuations in TL, which depend on range-dependent environmental properties that are aliased by the measurements. However, for receptions from all five sources, the modeled data capture the seasonal changes in TL as well as the statistics of the short-time fluctuations.

A. Environmental inputs to the model

1. Range-dependent sound-speed profiles

Oceanographic measurements were sparsely collected at both the deep-water CANAPE and SW CANAPE sites. To create range-dependent water-column sound-speed fields that connect each of the SIO sources in the Canada Basin with the PECOS array on the Chukchi Shelf, it was necessary to extrapolate the limited oceanographic data set to areas where measurements do not exist.

Although ocean circulation models for this region exist (Duda, 2017; Nguyen *et al.*, 2012; Spall *et al.*, 2018), they have limitations of their own, and the simulated ocean temperature and salinity fields can vary widely between models (Aksenov *et al.*, 2015). Although the higher-resolution models are expected to perform better, a simplistic refinement of the model resolution can lead to stronger model biases. Additional causes for model divergence include the choice of mixing and advection schemes, lateral boundary conditions, and treatment of the oceanic bottom boundary layer as well as differences and atmospheric forcing as regulated by the sea ice cover (Aksenov *et al.*, 2015). Given the uncertainty in the model outputs, previous applications of acoustic propagation models to simulate measured data in Arctic environments have utilized measured sound-speed profiles (Freitag *et al.*, 2015; Graupe *et al.*, 2019; Hope *et al.*, 2017).

The acoustic propagation modeling used in this work also uses a data driven approach to simulate the range-dependent water-column sound-speed profiles. For each computation of the received acoustic time-series, the range- and depth-dependent water-column sound-speed field was constructed using temporally relevant measurements from the BGEP Mooring A to represent the propagation conditions in the Canada Basin and from UD1 to UD7 to represent the range-dependent sound-speed profile on the Chukchi Shelf. A significant limitation of this data set is that no observations were made over Chukchi Slope in the region where much of the seasonally upward refracting propagation is hypothesized to occur. For the modeling that follows, the boundaries of this region were defined based on hydrographic studies of the Chukchi slope current (Corlett and Pickart, 2017; Li *et al.*, 2019; Spall *et al.*, 2018; Stabeno *et al.*, 2018), which suggest its location overlaps the region measured by UD1–UD7 and establishes its outer boundary as 100 km offshore of the shelfbreak.

Despite the limitations of the data, a method was devised to construct range-dependent sound-speed profiles that are consistent with the measurements and the current understanding of the physical oceanography of the northern Chukchi and Beaufort Seas. The two-dimensional (2D) sound-speed field defined along the range-depth plane connecting each of the SIO sources to the PECOS array was divided into four domains, with each domain informed by different data sets or interpolation schemes. An example of the water-column sound-speed field for April 1, 2017, with the different domains labeled is shown in Fig. 9.

The first domain is characterized by ducted sound propagation and is made up of data measured by BGEP Mooring A. Range-dependent sound-speed profiles were derived from the temporal measurements by advecting the measured profile in space using the average Beaufort Gyre speed of 0.02 m/s. The sound speed in the second domain was constructed using the temporally relevant measurement UD1–UD7. The locations of UD1, UD2, UD3, UD5, and UD7 are indicated by the white triangles above the plot. The third domain is defined as the upper 140 m of the water column offshore of UD7. Within domains two and three, the sound speed profile is expected to show strong seasonal dependence influenced by the water masses advected by the slope current. Since no direct measurements were made within region three during CANAPE, the water column properties were extrapolated from the UD7. For the five locations marked by the black triangles in Fig. 9, the median sound speed for a 24-h period immediately following the signal transmission was used. To simulate range-dependence within this region, the sound speed profile for each marker location was calculated from different interleaving 5-h blocks within the 24-h period. A 2D interpolation was used for the fourth domain to accommodate the change in the depth of the Atlantic Layer between the measurements in the basin and on the shelf. Finally, all the profiles were interpolated onto a 1 km grid for use in Bellhop.

To account for the advection of PWW by the Chukchi slope current, and because oceanographic observations were only made in a single range-depth slice, the water-column properties making up domains two and three were temporally shifted to account for the lag in the seasonal increase in TL. This approach is based on the hypothesis that the water mass is being advected along the shelf by the Chukchi slope

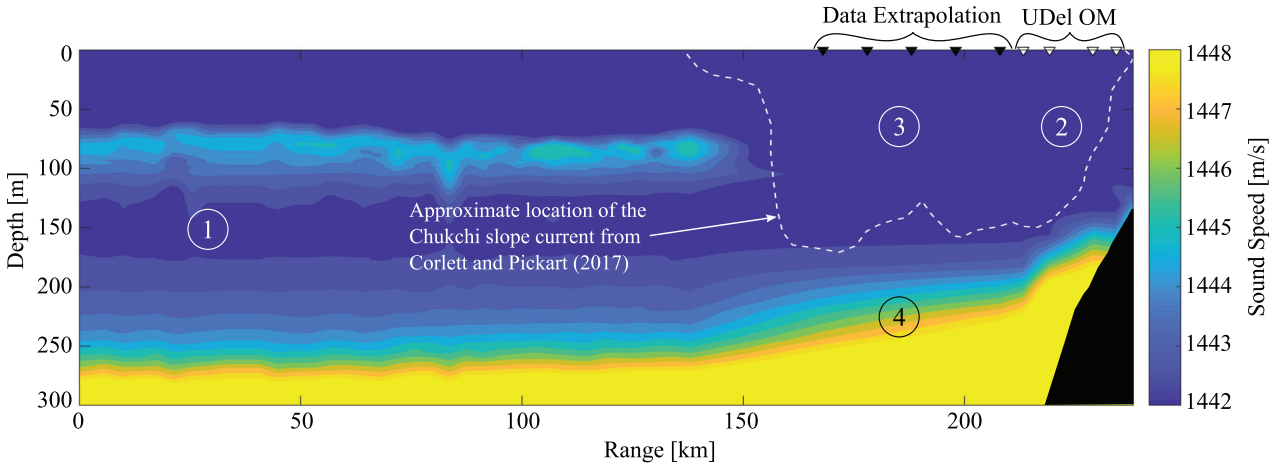

FIG. 9. (Color online) Water-column sound-speed field from the location of SIO 4 to PECOS constructed using measurements from April 1, 2017. The numbered markers represent regions informed by different data sets and/or interpolations.

current. The temporal shifts used for the water column properties are the lag times estimated from the TL data listed in Table II. For the propagation paths from SIO 2 and SIO 3, which are located to the east of the SIO 1 propagation path, negative temporal shifts were applied. For the propagation paths from SIO 4 and SIO 5, which are located to the west of the SIO propagation path, positive temporal shifts were applied. For the propagation path from SIO 1 to PECOS, which is within 9° of the line of bearing of UD1–UD7, no temporal shift was applied. The application of a uniform temporal shift to the 2D sound speed field is a coarse approximation of the advection of water by the slope current. However, given the numerous approximations made to reconstruct the sound speed field, a more complex interpolation scheme was not justified.

2. Range-dependent surface reflection coefficient

The surface reflection coefficient was calculated according to Eq. (1) using ULS data from the transceiver mooring associated with each source signal. To account for variable sea ice coverage over the acoustic propagation path, the sea ice concentration was taken into account using the MASAM2 database (Fetterer *et al.*, 2015). For seasonal periods of ice growth in October and November and ice melt in June and July, the range-dependent reflection coefficient $R_{total}(\sigma,f,r)$ was calculated from the range-independent reflection coefficient $R(\sigma,f)$ weighted by the range-dependent ice concentration $W(r)$ which is bounded between 0 (open water) and 1 (full ice cover),

$$R_{total}(\sigma,f,r) = R(\sigma,f)W(r). \quad (2)$$

B. Results

Examples showing environmental conditions and acoustic TL for three time periods are depicted in Fig. 10 to illustrate different propagation regimes that occurred over the course of the yearlong experiment. The model inputs are spatially interpolated range-dependent sound-speed profiles and sea ice conditions for the propagation path from SIO 4 to PECOS, and the calculated TL is for the SIO 4 center frequency of 275 Hz. For all three cases, the sound-speed profile in the basin (0–150 km in range) exhibits a sound speed minimum capable of supporting ducted propagation. Range-dependent features in the basin profiles can be observed, including both upper and lower halocline eddies as well as variability in the sound speed of the PSW. Nevertheless, ducted propagation with the basin is supported as demonstrated by the TL calculations in Figs. 10(d)–10(f). For the open-water condition [see Fig. 10(d)], significant energy is observed outside of the Beaufort Duct due to sound that is refracted upward in the Atlantic Layer and reflects from the loss-less sea surface. For the ice-covered cases [see Figs. 10(e)–10(f)], these paths are attenuated through interaction with the rough sea ice boundary.

More seasonal variability is observed in the water-column sound-speed profiles on the shelf and slope. During open-water conditions [see Fig. 10(a)], PSW is typically present in the upper 100 m of the water column on the shelf and slope. Although the duct is discontinuous, especially within the last 50 km of the propagation path, TL remains relatively low due to the loss-less reflection from the water-air interface. The two cases shown for the ice-covered months [see Figs. 10(e) and 10(f)] reveal dramatically different TL levels on the shelf. In February, PSW is still present on the slope and shelf, and ducted propagation is observed throughout the entirety of the propagation path [see Fig. 10(e)]. In March, WW has been advected over the slope, and upward refracting conditions are observed over the last 100 km of the propagation path. In this case, sound which was ducted in the basin becomes surface interacting around a range of 150 km, and the TL increases rapidly at this range [see Fig. 10(f)]. Sea ice conditions are similar between these two cases, and the difference in TL is attributed to the changes in the water-column sound-speed profile.

Comparisons of the measured and modeled RL and time-series data for propagation from SIO 1 to PECOS are shown in Fig. 11. As shown in Fig. 11(a), the model produces a fair representation of the peak RL throughout the

https://doi.org/10.1121/10.0001970

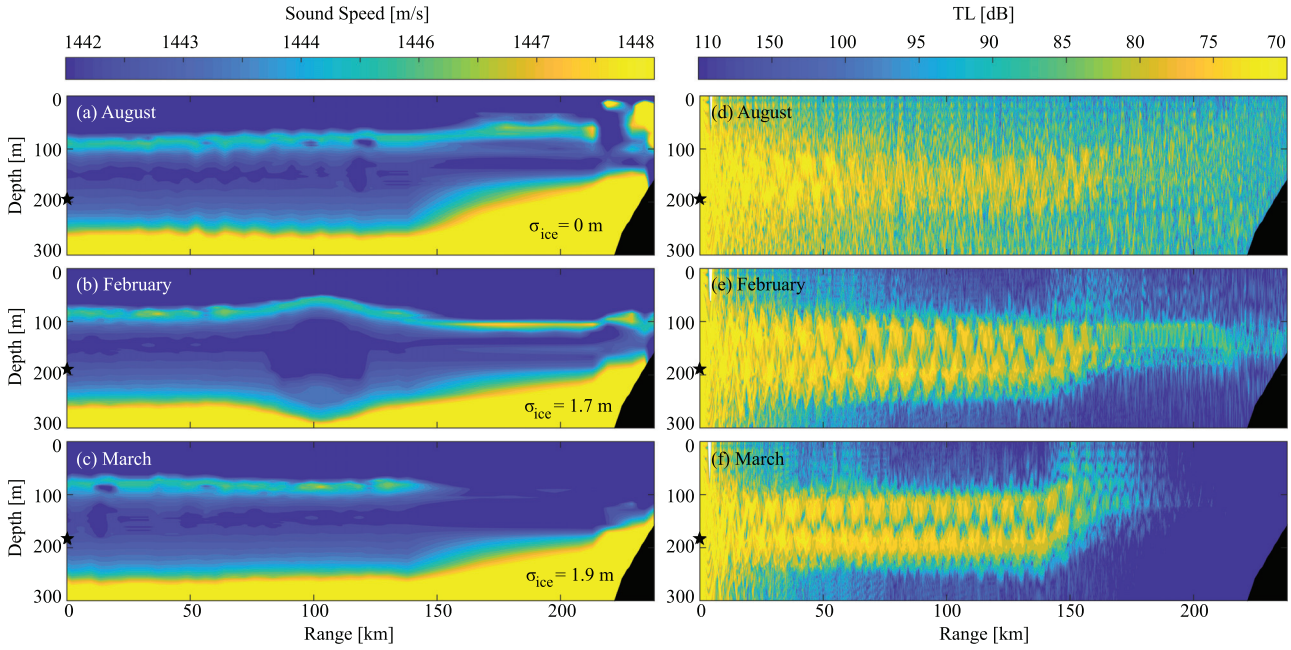

FIG. 10. (Color online) Examples of range-dependent sound speed profiles and sea ice roughness (represented by the standard deviation of the sea ice draft σ_{ice}) for three different propagation regimes observed during different seasons over the course of SW CANAPE: (a) open-water propagation during the month of August, (b) ducted sound propagation during the month of February, and (c) upward refracting on the slope during the month of March. (d)–(f) Corresponding TL calculations at a frequency of 250 Hz. In all figures, the source depth is indicated by the black star at 0 km in range, and the bathymetry of the shelf is shown in by the black triangular feature between 220 and 235 km in range.

yearlong experiment, including the rapid increase in TL during the month of March and the decrease in TL during the month of July. For both of these events, the timing of the event and the rate of change in TL in the modeled data are in good agreement with that of the measured data. The advection of water masses by the slope current is not included in the modeling for SIO 1 since the acoustic propagation path is roughly aligned with the line of bearing of UD1–UD 7 (within 9°). During the months of April, May, and June, when TL is greatest, there are fewer observations of the measured signal. During this time period, the modeled RL is often more than 40 dB below the measured ambient noise level.

Monthly averages of the beamformed, pulse-compressed waveforms are shown in Fig. 11(b) with the shaded area indicating one standard deviation around the mean. The modeled data were temporally shifted to align the mean peak RL of the modeled data with that of the measurement for each month. There is good agreement in the relative timing of both the surface reflected and ducted arrivals. However, the modeled data do not faithfully represent the relative amplitudes of the arrivals during the ice covered months. The surface reflected arrival incurs too much loss, and the ducted arrival incurs too little loss. This is also evident in the peak RL data in Fig. 11(a) during the months of January and February, for which the modeled data have a greater peak RL than the measured data. The disagreement is primarily attributed to the inability of ray theory to model energy leakage of the low-frequency signals in the Beaufort Duct. Inaccuracies in the range-dependent environmental inputs to the model may also play a role, specifically the extrapolated region representing the location of the Chukchi Slope Current.

The dependence of the calculated RL on acoustic ducting on the slope and on surface loss are further examined in Fig. 12. The RL data plotted on the *y*-axis are the same data points shown as a function of time in Fig. 11. This discussion adds to the observations in Sec. III C, which qualitatively described temporal correlations between the onset of increased TL with temperature measurements on the shelf and slope and the decrease in TL with the ULS ice thickness measurements. Examining the model inputs in relation to the calculated RL provides insight into the interrelationship between the water-column sound-speed field and sea ice cover on TL.

First, consider the effect of water column sound speed on RL as shown in Fig. 12(a). Since the water column properties on the shelf and slope have been identified as having the dominant influence of the seasonal increase in TL, only the sound speed data from the last 100 km of the propagation are considered. To reduce the range- and depth-dependent sound speed field within this region to a single value, the maximum temperature in the upper 125 m of the water column was monitored because this feature controls whether the sound propagation is ducted. Next, the median value was taken over range as the representative sound speed. Lower values indicate the weakening or absence of ducted propagation, which is the condition that results in increased TL due to the interaction of sound with the ice cover.

During the beginning of the experiment, relatively slow sound speeds are observed in the upper water column, but

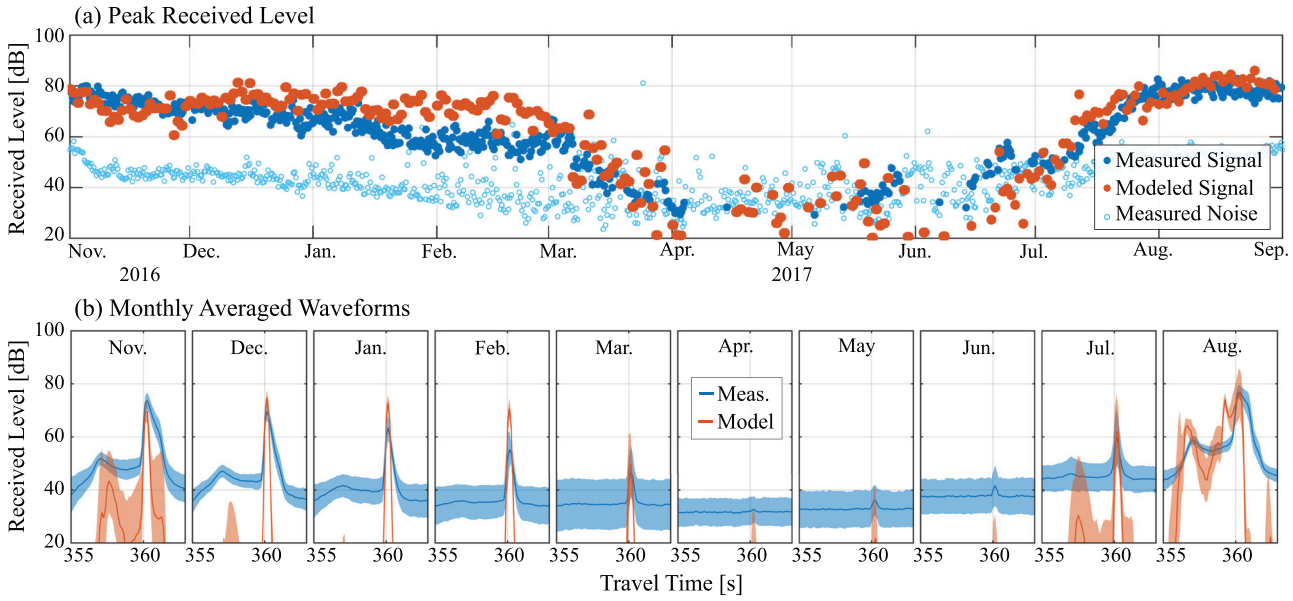

FIG. 11. (Color online) (a) Comparison of measured and modeled peak RL for receptions from SIO 1. (b) Comparison of measured and modeled beam-formed, pulse-compressed data for each month of the experiment. The line is the monthly mean of the data, and the shaded areas represent one standard deviation around the mean.

high RL are maintained because surface loss is low. Through the early winter, warmer waters fill the upper water column, which partially insulates sound from the ice cover. Near the end of February, the sound speed on the slope begins to decrease, which causes a decrease in the RL. This trend continues until the end of March, and the data during this period are highlighted by the black circles. The RL remains low until the end of July, when the RL is observed to increase independent of sound speed. Around July 10, PSW water arrives in the shelf and slope, and the median sound speed in the upper 125 m abruptly increases. However, by this time, the sea ice cover is no longer present, and the RL is not strongly influenced by the water column properties.

Next, consider the effect of surface loss on RL as depicted in Fig. 12(b). For cases where the surface loss was range-dependent, the mean value of surface loss along the propagation path was used for the comparison. The highest RL is observed during the beginning and end of the experiment when the surface loss is less than 1 dB. As the ice thickens in the winter, the surface loss increases to a value of approximately 1.75 dB in February, with only a slight decrease observed in the associated in RL. Around mid-March, surface loss takes on a nearly constant value of 2 dB for the remainder of the winter season. During this period, RL decreases independent of changes in the surface loss, as the water column properties are primarily responsible for the observed changes in RL. During the ice melt season, highlighted by the black circles, the RL shows a strong dependence on surface loss. During this period, the water column sound speed profile on the shelf and slope is upward refracting, and surface loss is controlling TL. Finally, the highest RL are observed in August during the open water condition.

Figure 13 compares the measured and modeled peak RL for receptions from all five SIO sources. Two calculations of the modeled RL are shown: one that accounts for advection of the PWW by the slope current using the temporal shifts listed in Table II, and another that neglects the temporal shifts and uses the same time samples of the water-column sound-speed properties to calculate sound propagation from all five sources. For both calculations, there are times

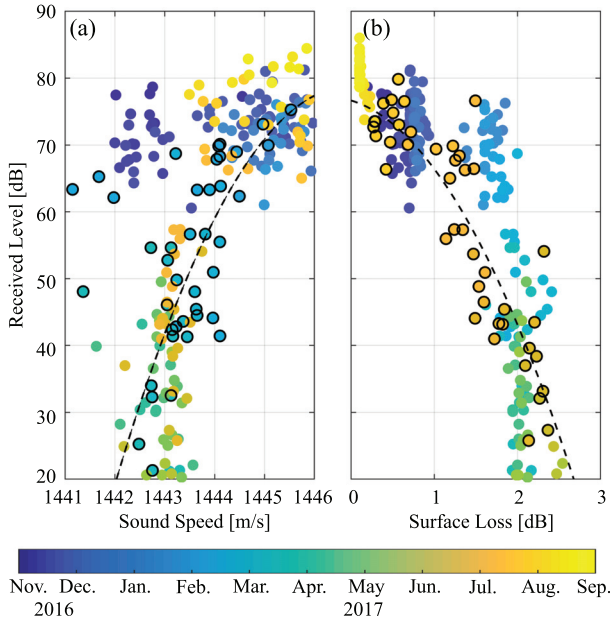

FIG. 12. (Color online) The dependence of RL calculated for SIO 1 on (a) ducting on the slope and (b) surface loss. The color represents time of the year and the black circles highlight the period on increasing TL from February 20 to March 31 in (a) and the period of decreasing TL from June 20 to July 31 in (b). The dashed lines are a second order fit to the highlighted data.

https://doi.org/10.1121/10.0001970

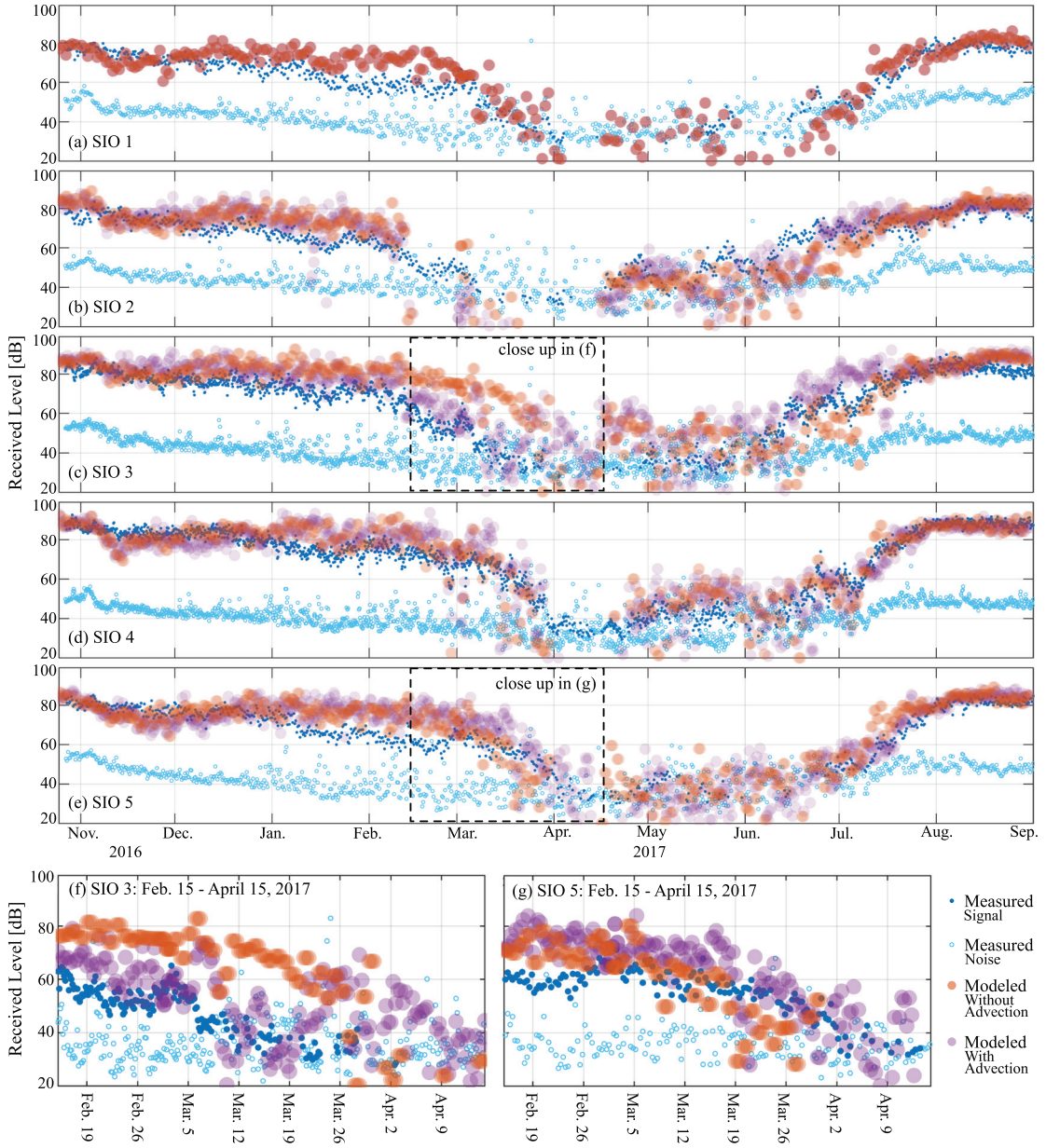

FIG. 13. (Color online) (a)–(e) Comparison between modeled and measured peak RL for receptions from all five SIO sources. Two calculations of the modeled RL are shown: one that accounts for advection of the PWW by the slope current, and another that neglects the temporal shifts. (f)–(g) Comparisons of the two calculations of RL with the measured data for SIO 3 and SIO 5 for the time period of increasing TL. These data most clearly show the impact of the advection of WW over the slope.

throughout the year when the model overestimates or underestimates TL. As discussed in the context of Fig. 11, the discrepancies between measured and modeled RL are attributed to assumptions made within the acoustic propagation model as well as uncertainties in the environmental inputs. There are distinct periods outside of the period of maximum TL (nominally April through June), for which the modeled RL is lower than the 20 dB limit of the plot (i.e., mid-February to mid-April for SIO 2, and late March to late April for SIO 4). These periods correspond to times when currents pulled the mooring cable down so that the source was no longer in the sound speed duct (see Fig. 2). The model overestimates TL during these periods.

For propagation from SIO 1 to PECOS, no temporal shift was applied to the water column sound speed inputs for either modeled case since the propagation path is roughly aligned with the line of bearing of UD1–UD 7 (within 9°). As discussed in the context of Fig. 11, comparison with the measured data shows good agreement in both the timing and magnitude of the seasonal increase and decrease in TL. For SIO 2 and SIO 4, the depth of the source influences the increase in TL in February and March, and the propagation effects caused by the advection of WW by the slope current cannot be readily observed. Comparisons of the two calculations of RL with the measured data for SIO 3 and SIO 5 most clearly show the impact of the advection of WW over

the slope. Closeup views highlighting the time period of increasing TL for these receptions are shown in Figs. 11(f) and 11(g). For SIO 3, the calculation that neglects the temporal shift in water column inputs (orange circles) causes the seasonal increase in TL to occur approximately three weeks late, and for SIO 5, it occurs almost two weeks early. Conversely, the solutions that include the temporal shifts in water column inputs (purple circles) agree well with the measured data. These results support the hypothesis that the increase in TL February and March is caused by the advection of WW by the slope current, which produces an upward refracting sound-speed profile over the shelf.

The decrease in TL associated with the ice melt in June and July is also captured by the modeled data. During this period, the flow of the slope current is an order of magnitude faster (Stabeno *et al.*, 2018), and the temporal shifts in water column inputs (purple circles) do not apply. However, since the acoustic propagation conditions during this time period are primarily driven by the retreating ice cover, there is close agreement in the RL predicted by both calculations.

For receptions from all sources, the model reproduces the shorter timescale fluctuations including decreases in TL for week- to month-long periods between April and June. The data also show variations in the RL from one reception to the next that range of up to 10 dB, consistent with the measured data. These changes are due to the fluctuations in both the water-column sound-speed profile and surface loss.

V. CONCLUSIONS

The Pacific Arctic Region is undergoing dramatic changes in environmental conditions, including a decline in the sea-ice cover and changes to the thermohaline structure. The results in this paper show that acoustic propagation from deep to shallow water is sensitive to variations in these parameters, and TL can be used to remotely sense these changes in the environment. Specifically, measurements of long-range acoustic propagation from the Canada Basin to the Chukchi Shelf showed a seasonal pattern of TL that could be related to the outflow of the Chukchi Slope Current and the retreat of the ice cover. However, due to the lack of direct measurements of the ocean temperature and salinity on the Chukchi Slope, the proposed relationship could not be verified by independent measurements. Furthermore, this data set represents the conditions observed over a single yearlong period in the Canada Basin and Chukchi Shelf. Additional measurements are needed to understand interannual changes in environmental conditions. Acoustic measurements can play an important role in remote monitoring systems to characterize this rapidly transitioning environment and assess the Arctic's role in climate change.

This study hypothesized that the sudden increase in TL during early spring was related to the advection of cold water by the Chukchi Slope Current westward. The arrival of WW on the shelf created an upward refraction sound speed profile that resulted in increased interaction of sound with the sea ice canopy. This produced increased TL through scattering of sound away from specular angles and conversion to shear waves in the sea ice. Additionally, the relative timing of the onset of the increase in TL from the SIO sources positioned in the basin was used to estimate the speed of the Chukchi Slope Current. The estimated current speed of 1.7 cm/s was consistent with other data sets. Furthermore, this study hypothesized that the decrease in TL in the summer was linked to breakup of the ice cover. A large localized polynya opened by winds in the southeastern Beaufort Sea caused a large crack to develop that extended from the Beaufort to the Lincoln Sea. No longer attached to the shoreline of the Canadian Arctic Archipelago, the ice rotated with the Beaufort Gyre. This motion exposed the easternmost SIO moorings to open water conditions first. With open water above the propagation path, TL was reduced.

These interpretations were supported by results from a ray-based acoustic propagation model that provided good agreement in both the timing and magnitude of the seasonal changes in TL. However, the modeling involved a number of assumptions, including extrapolation of the oceanographic data and simplified modeling of the surface loss from the ice cover. The modeling approach presented in this work was sufficient to quantify the observations, an alternative approach based on a physics-based, coupled ice-ocean model of this region could support reconstruction of time- and range-dependent environmental input parameters. However, such a model would need to include details of the depth-dependent temperature and salinity structure which compose the sound-speed duct as well as mesoscale features such as the Chukchi Slope Current. Additionally, a more sophisticated acoustic modeling approach capable of modeling the interaction of sound with the complex elastic sea ice canopy would provide a more faithful reconstruction of the measured data. However, the application of a more computationally intensive acoustic propagation model would need to be justified by higher fidelity model inputs from oceanographic models.

ACKNOWLEDGMENTS

This work was supported by the Office of Naval Research Ocean Acoustics Program (ONR OA322) under Grant Nos. N00014-15-1-2144, N00014-15-1-2119, N00014-15-1-2017, N00014-15-1-2068, N00014-15-1-2110, N00014-19-1-2721, N00014-15-1-2898, N00014-15-1-2806, and N00014-18-1-2140. The basin moored environmental data were supported by the ONR Arctic and Global Prediction Program (ONR AG322) under Grant No. N00014-15-1-2782. Mooring and hydrographic data were collected and made available by the Beaufort Gyre Exploration Program based at the Woods Hole Oceanographic Institution (http://www.whoi.edu/beaufortgyre) in collaboration with researchers from Fisheries and Oceans Canada at the Institute of Ocean Sciences. The ITP data were collected and made available by the ITP Program (Krishfield *et al.*, 2008; Toole *et al.*, 2011) based at the Woods Hole Oceanographic Institution (http://www.whoi.edu/itp). We

acknowledge the use of imagery from the Worldview Snapshots application (https://wvs.earthdata.nasa.gov), part of the Earth Observing System Data and Information System (EOSDIS).

Aksenov, Y., Karcher, M., Proshutinsky, A., Gerdes, R., de Cuevas, B., Golubeva, E., Kauker, F., Nguyen, A. T., Platov, G. A., Wadley, M., Watanabe, E., Coward, A. C., and Nurser, A. J. G. (**2015**). "Arctic pathways of Pacific Water: Arctic ocean model intercomparison experiments," J. Geophys. Res. Oceans **121**, 27–59, https://doi.org/10.1002/2015JC011299.

Badiey, M., Muenchow, A., Wan, L., Ballard, M. S., Knobles, D. P., and Sagers, J. D. (**2014**). "Modeling three dimensional environment and broadband acoustic propagation in arctic shelf-basin region," J. Acoust. Soc. Am. **136**(4), 2317.

Badiey, M., Wan, L., Pecknold, S., and Turgut, A. (**2019**). "Azimuthal and temporal sound fluctuations on the Chukchi Continental Shelf during the Canada Basin Acoustic Propagation Experiment 2017," J. Acoust. Soc. Am. **146**(6), EL530–EL536.

Ballard, M. S. (**2019**). "Three-dimensional acoustic propagation effects induced by the sea ice canopy," J. Acoust. Soc. Am. **146**(4), EL364–EL368.

Ballard, M. S., Badiey, M., Sagers, J. D., Colosi, J., Turgut, A., Pecknold, S., Proshutinsky, A., Krishfield, R., Worcester, P. F., and Dzieciuch, M. A. (**2019**). "A study on the yearlong record of sound propagation from the Canada Basin to the Chukchi Shelf," in *Proceedings of the Underwater Acoustics Conference and Exhibition*, June 30–July 5, Crete, Greece.

Brugler, E. T., Pickart, R. S., Moore, G. W. K., Roberts, S., Weingartner, T. J., and Statscewich, H. (**2014**). "Seasonal to interannual variability of the Pacific water boundary current in the Beaufort Sea," Prog. Oceanogr. **127**(0), 1–20.

Collins, M. D. (**2015**). "Treatment of ice cover and other thin elastic layers with the parabolic equation method," J. Acoust. Soc. Am. **137**(3), 1557–1563.

Collis, J. M., Frank, S. D., Metzler, A. M., and Preston, K. S. (**2016**). "Elastic parabolic equation and normal mode solutions for seismo-acoustic propagation in underwater environments with ice covers," J. Acoust. Soc. Am. **139**(5), 2672–2682.

Collins, M. D., Turgut, A., Menis, R., and Schindall, J. A. (**2019**). "Acoustic recordings and modeling under seasonally varying sea ice," Sci. Rep. **9**, 1–11.

Colosi, J. A., Kucukosmanoglu, M., Worcester, P. F., Dzieciuch, M., Proshutinsky, A. Y., Krishfield, R. A., and Nash, J. D. (**2018**). "An overview of Beaufort Sea eddies, internal waves, and spice from several recent field efforts and implications for acoustic propagation," J. Acoust. Soc. Am. **144**(3), 1665–1665.

Corlett, W. B., and Pickart, R. S. (**2017**). "The Chukchi slope current," Prog. Oceanogr. **153**, 50–65.

Diachok, O. I. (**1976**). "Effects of sea-ice ridges on sound propagation in the Arctic Ocean," J. Acoust. Soc. Am. **59**(5), 1110–1120.

Duda, T. F. (**2017**). "Acoustic signal and noise changes in the Beaufort Sea Pacific Water duct under anticipated future acidification of Arctic Ocean waters," J. Acoust. Soc. Am. **142**(4), 1926–1933.

Duda, T. F., Zhang, W. G., Lin, Y. T., and Newhall, A. E. (**2019**). "Long-range sound propagation in the Canada Basin," *Proceedings of the Underwater Acoustics Conference and Exhibition*, June 30–July 5, Crete, Greece.

Fetterer, F., Stewart, J. S., and Meier, W. (**2015**). "MASAM2: Daily 4 km Arctic Sea Ice Concentration, Version 1," National Snow & Ice Data Center, http://doi.org/10.7265/N5ZS2TFT.

Freitag, L., Ball, K., Partan, J., Koski, P., and Singh, S. (**2015**). "Long range acoustic communications and navigation in the Arctic," in *Proceedings of IEEE/MTS Oceans 2015*, October 19–22, Washington, DC.

Frey, K. E., Moore, G., Cooper, L. W., and Grebmeier, J. M. (**2015**). "Divergent patterns of recent sea ice cover across the Bering, Chukchi, and Beaufort Seas of the Pacific Arctic Region," Prog. Oceanogr. **136**, 32–49.

Frick, J. R. (**1991**). "Acoustic scattering from elastic ice: A finite difference solution," Ph.D. thesis, Woods Hole Oceanographic Institution Massachusetts Institue of Technology, Woods Hole, MA.

Gavrilov, A. N., and Mikhalevsky, P. N. (**2006**). "Low-frequency acoustic propagation loss in the Arctic Ocean: Results of the Arctic climate observations using underwater sound experiment," J. Acoust. Soc. Am. **119**(6), 3694–3706.

Gordon, D. F., and Bucker, H. P. (**1984**). "Arctic acoustic propagation model with ice scattering," Technical Report 985 (Naval Ocean Systems Center, San Diego, CA).

Graupe, C. E., Uffelen, L. J. V., Webster, S. E., Worcester, P. F., and Dzieciuch, M. A. (**2019**). "Preliminary results for glider localization in the Beaufort Duct using broadband acoustic sources at long range," in *Proceedings of MTS/IEEE Oceans 2019*, October 27–31, Seattle, WA.

Hope, G., Sagen, H., Storheim, E., HobAk, H., and Freitag, L. (**2017**). "Measured and modeled acoustic propagation underneath the rough Arctic sea-ice," J. Acoust. Soc. Am. **142**(3), 1619–1633.

Krishfield, R. A., Proshutinsky, A., Tateyama, K., Williams, W. J., Carmack, E. C., McLaughlin, F. A., and Timmermans, M. L. (**2014**). "Deterioration of perennial sea ice in the Beaufort Gyre from 2003 to 2012 and its impact on the oceanic freshwater cycle," J. Geophys. Res. Oceans **119**(2), 1271–1305, https://doi.org/10.1002/2013JC008999.

Krishfield, R., Toole, J., Proshutinsky, A., and Timmermans, M. L. (**2008**). "Automated ice-tethered profilers for seawater observations under pack ice in all seasons," J. Atmos. Oceanic Technol. **25**(11), 2091–2105.

Kudryashov, V. M. (**1996**). "Sound reflection from ice cover," Acoust. Phys. **42**, 215–221.

LePage, K., and Schmidt, H. (**1994**). "Modeling of low-frequency transmission loss in the central Arctic," J. Acoust. Soc. Am. **96**(3), 1783–1795.

Li, M., Pickart, R. S., Spall, M. A., Weingartner, T. J., Lin, P., Moore, G., and Qi, Y. (**2019**). "Circulation of the Chukchi Sea shelfbreak and slope from moored timeseries," Prog. Oceanogr. **172**, 14–33.

Lynch, J. F., Gawarkiewicz, G. G., Lin, Y. T., Duda, T. F., and Newhall, A. (**2018**). "Impacts of ocean warming on acoustic propagation over continental shelf and slope regions," Oceanography **31**(2), 174–181.

McCammon, D. F., and McDaniel, S. T. (**1985**). "The influence of the physical properties of ice on reflectivity," J. Acoust. Soc. Am. **77**(2), 499–507.

Nguyen, A. T., Kwow, R., and Menemenlis, D. (**2012**). "Source and pathway of the Western Arctic upper halocline in a data-constrained coupled ocean and sea ice model," J. Phys. Oceanogr. **42**, 802–823.

Porter, M. B., and Bucker, H. P. (**1987**). "Gaussian beam tracing for computing ocean acoustic fields," J. Acoust. Soc. Am. **82**(4), 1349–1359.

Proshutinsky, A., Krishfield, R., and Timmermans, M. L. (**2020**). "Introduction to special collection on arctic ocean modeling and observational synthesis (FAMOS) 2: Beaufort Gyre phenomenon," J. Geophys. Res. Oceans **125**(2), e2019JC015400, https://doi.org/10.1029/2019JC015400.

Proshutinsky, A., Krishfield, R., Toole, J. M., Timmermans, M. L., Williams, W., Zimmermann, S., Yamamoto-Kawai, M., Armitage, T. W. K., Dukhovskoy, D., Golubeva, E., Manucharyan, G. E., Platov, G., Watanabe, E., Kikuchi, T., Nishino, S., Itoh, M., Kang, S. H., Cho, K. H., Tateyama, K., and Zhao, J. (**2019**). "Analysis of the Beaufort Gyre freshwater content in 2003–2018," J. Geophys. Res. Oceans **124**(12), 9658–9689, https://doi.org/10.1029/2019JC015281.

Sagers, J. D., Ballard, M. S., and Badiey, M. (**2015**). "Investigating the effects of ocean layering and sea ice cover on acoustic propagation in the Beaufort Sea," Proc. Mtg. Acoust. **25**(1), 005003.

Siderius, M., Porter, M. B., Hursky, P., and McDonald, V. (**2007**). "Effects of ocean thermocline variability on noncoherent underwater acoustic communications," J. Acoust. Soc. Am. **121**(4), 1895–1908.

Simon, B., Isakson, M. J., and Ballard, M. S. (**2018**). "Modeling acoustic wave propagation and reverberation in an ice covered environment using finite element analysis," Proc. Mtg. Acoust. **33**(1), 070002.

Spall, M. A., Pickart, R. S., Li, M., Itoh, M., Lin, P., Kikuchi, T., and Qi, Y. (**2018**). "Transport of Pacific Water into the Canada Basin and the formation of the Chukchi Slope Current," J. Geophys. Res. Oceans **123**(10), 7453–7471, https://doi.org/10.1029/2018JC013825.

Stabeno, P., Kachel, N., Ladd, C., and Woodgate, R. (**2018**). "Flow patterns in the Eastern Chukchi Sea: 2010–2015," J. Geophys. Res. Oceans **123**(2), 1177–1195, https://doi.org/10.1002/2017JC013135.

Strub-Klein, L., and Sudom, D. (**2012**). "A comprehensive analysis of the morphology of first-year sea ice ridges," Cold Regions Sci. Technol. **82**, 94–109.

Timmermans, M. L., Toole, J., and Krishfield, R. (**2018**). "Warming of the interior Arctic Ocean linked to sea ice losses at the basin margins," Sci. Adv. **4**(8), eaat6773.

Timmermans, M. L., Toole, J., Proshutinsky, A., Krishfield, R., and Plueddemann, A. (**2008**). "Eddies in the Canada Basin, Arctic Ocean, observed from ice-tethered profilers," J. Phys. Oceanogr. **38**(1), 133–145.

Toole, J. M., Krishfield, R. A., Timmermans, M. L., and Proshutinsky, A. (**2011**). "The ice-tethered profiler: Argo of the arctic," Oceanography **24**, 126–135.

Twersky, V. (**1957**). "On scattering and reflection of sound by rough surfaces," J. Acoust. Soc. Am. **29**(2), 209–225.

Wood, K. R., Bond, N. A., Danielson, S. L., Overland, J. E., Salo, S. A., Stabeno, P. J., and Whitefield, J. (**2015**). "A decade of environmental change in the Pacific Arctic region," Prog. Oceanogr. **136**, 12–31.

Woolfe, K., Collins, M. D., Calvo, D. C., and Siegmann, W. L. (**2016**). "Seismo-acoustic benchmark problems involving sloping fluid-solid interfaces," J. Comput. Acoust. **24**(04),1650022.

Zhao, M., Timmermans, M. L., Cole, S., Krishfield, R., Proshutinsky, A., and Toole, J. (**2014**). "Characterizing the eddy field in the Arctic Ocean halocline," J. Geophys. Res. Oceans **119**(12), 8800–8817, https://doi.org/10.1002/2014JC010488.

Zhong, W., Steele, M., Zhang, J., and Cole, S. T. (**2019**). "Circulation of Pacific Winter Water in the western Arctic Ocean," J. Geophys. Res. Oceans **124**(2), 863–881, https://doi.org/10.1029/2018JC014604.